Neurophysiological trajectories in Alzheimer's disease progression

Kiwamu Kudo[1,2,*], Kamalini G. Ranasinghe[3], Hirofumi Morise[1,2], Faatimah Syed[3], Kensuke Sekihara[4], Katherine P. Rankin[3], Bruce L. Miller[3], Joel H. Kramer[3], Gil D. Rabinovici[3,5], Keith Vossel[3,6], Heidi E. Kirsch[1], and Srikantan S. Nagarajan[1]

[1]Biomagnetic Imaging Laboratory, Department of Radiology and Biomedical Imaging, University of California, San Francisco, CA, 94143, USA

[2]Medical Imaging Business Center, Ricoh Company, Ltd., Kanazawa, 920-0177, Japan

[3]Memory and Aging Center, UCSF Weill Institute for Neurosciences, University of California, San Francisco, CA, 94158, USA.

[4]Signal Analysis Inc., Hachioji, Tokyo, 192-0031, Japan

[5]Department of Radiology and Biomedical Imaging, University of California, San Francisco, CA, 94143, USA

[6]Mary S. Easton Center for Alzheimer's Research and Care, Department of Neurology, David Geffen School of Medicine, University of California Los Angeles, Los Angeles, CA 90095, USA

[*]kiwamu.kudo@jp.ricoh.com

Abstract

Alzheimer's disease (AD) is characterized by accumulation of amyloid-β and misfolded tau proteins causing synaptic dysfunction and progressive neurodegeneration and cognitive decline. Altered neural oscillations have been consistently demonstrated in AD. However, the trajectories of abnormal neural oscillations in AD progression and their relation to neurodegeneration and cognitive decline are unknown. We deployed robust event-based sequencing models (EBM) to investigate trajectories of long-range and local neural synchrony across AD stages, estimated from resting-state magnetoencephalography. Synchrony increases in delta-theta and decreases in alpha and beta bands showed progressive changes along the EBM stages of AD. Decreases in alpha and beta synchrony preceded both neurodegeneration and cognitive decline, indicating that frequency-specific neuronal synchrony abnormalities are early manifestations of AD pathophysiology. Long-range synchrony effects were larger than local synchrony, indicating greater sensitivity of connectivity metrics involving multiple brain regions. These results demonstrate the evolution of functional neuronal deficits along the sequence of AD progression.

Introduction

Alzheimer's disease (AD) is a neurodegenerative disease characterized by amyloid-β (Aβ) plaques and neurofibrillary tangles of abnormally phosphorylated tau[1]. Clinical and epidemiological studies have suggested that Aβ accumulation occurs very early in the timeline of AD neuropathological changes, likely preceding the accumulation of tau, and subsequent neurodegeneration and cognitive decline[2,3]. AD neuropathological changes are therefore described as a continuum, starting from the presymptomatic stage of proteinopathy and continues to progress during the symptomatic stage with increasing stages of disease severity[3,4]. Transgenic mouse models of AD have shown that AD proteinopathy of Aβ and tau is associated with synaptic and circuit dysfunctions within neural networks[5–7]. However, the temporal change in synaptic and circuit dysfunction along disease progression in patients with AD remains largely unknown.

Functional deficits in neural networks, especially in the presymptomatic stage, have attracted attention in recent years with the rapidly evolving landscape of plasma-biomarkers of early detection and the novel therapeutics showing the benefits of early intervention[8]. Abnormal synchrony of neural oscillations, indeed, has been reported not only in patients along the clinical AD spectrum including mild cognitive impairment (MCI) due to AD and AD-dementia[9–17] but also during the preclinical stages of AD[13,18]. Neuronal oscillations from non-invasive electrophysiological measures such as electroencephalography (EEG) and magnetoencephalography (MEG), represent the synchronized activity of excitatory and inhibitory neurons, and thus provide sensitive indices of altered neuronal and circuit functions in AD. As synaptic dysfunction is strongly associated with AD proteinopathy, altered synchrony of neural oscillations may essentially capture the early functional deficits of neural networks even before the clinical symptoms emerge. However, it remains unknown which neurophysiological signature changes capture such deficits and the temporal evolution of these changes along the timeline of preclinical to MCI to AD dementia stages in clinical populations.

In this study we investigated the trajectories of neurophysiological changes along the course of clinical AD progression, by examining long-range and local neural synchrony patterns in the resting brain. We hypothesized that frequency-specific long-range and local synchrony abnormalities in neuronal oscillations may precede both neurodegeneration and cognitive deficits in AD. To examine the temporal relationship amongst altered neural synchrony, neurodegeneration, and cognitive deficits, we used data-driven disease progression models–event-based sequencing models (EBMs), which have been successfully used to predict AD progression from cross-sectional biomarker data[19–21]. In an EBM, disease progression is described as a series of discrete events, defined as the occurrence of a particular biomarker reaching a threshold abnormal value, and the estimated likelihood of temporal

sequence of events defines the disease trajectory. We developed and employed a robust EBM framework that is less sensitive to abnormal threshold determinants and hence with unbiased subject assignments to disease stages.

Specifically, leveraging the high spatiotemporal resolution of MEG imaging, we examined two neuronal oscillatory synchrony metrics–cross-regional amplitude-envelope correlation (AEC) and regional power spectral density (PSD). The AEC and PSD quantify long-range and local neural synchrony, respectively. Recent test-retest studies of MEG resting-state metrics have revealed that both metrics are indeed highly reliable[22,23]. To evaluate the frequency specificity of neurophysiological trajectories, three canonical frequency bands, delta-theta (2–7 Hz), alpha (8–12 Hz), and beta (15–29 Hz) bands, were considered. For metrics of neurodegeneration and global cognitive ability, we respectively chose the parahippocampal gyrus (PHG) volume and mini mental state examination (MMSE) score for each participant. Neurodegeneration, which is related to neuronal loss as well as synaptic loss and synapse dysfunction[24,25], is macroscopically detectable as brain atrophy in magnetic resonance imaging (MRI), and thus we evaluated neurodegeneration as loss of grey matter, specifically PHG volume loss, using each participant's T1 MRI. We first deployed an Atrophy-Cognition EBM (AC-EBM) with only the neurodegeneration and cognitive decline measures, and then examined metrics of long-range and local synchrony of neuronal oscillations corresponding to each estimated disease stage. Next, we deployed two separate Synchrony-Atrophy-Cognition EBMs (SAC-EBMs) which respectively included long-range or local neural synchrony measures along with PHG volume and global cognition to investigate how the synchrony metrics stratify AD progression. Consistent with our hypothesis, we found that both long-range and local neural synchrony in alpha and beta bands, but not in the delta-theta band, become abnormal at the earliest preclinical stages of AD, preceding both neurodegeneration and cognitive deficits.

Results

Participant demographics

[Figure 1 about here.]

This study included a well-characterized cohort of 78 patients with AD (50 female; 28 male) including 35 patients with AD dementia and 43 patients with MCI due to AD. We also included 70 cognitively-unimpaired older adults as controls (41 female; 29 male). The Clinical Dementia Rating (CDR) scales were 0 for cognitively unimpaired controls, 0.5 for the patients with MCI, and 1 $(n = 27)$ or 2 $(n = 8)$ for the patients with AD dementia. There was no difference in sex distribution between AD and control groups [$\chi^2(1) = 0.477$; $p = 0.49$]. Average age at the time of the MEG was slightly higher in the control group than patients with AD (controls, mean±SE: 70.5 ± 0.99, range: 49.5–87.7; AD, mean±SE: 63.9 ± 1.01, range: 49.0–84.4) [unpaired t-test: $t(146) = -4.708$;

$p < 0.001$]. Average MMSE in patients with AD was 22.7 ± 0.43 while the average MMSE in the controls was 29.2 ± 0.48 (Fig. 1c). The MMSE scores were adjusted for covariates of age and the time-difference between MMSE administration and MEG scan using a general linear model (GLM). MMSE-decline z-scores, z_{MMSE} were then computed for each subject (Fig. 1d), standardized by the adjusted MMSE scores of the control group and sign-inverted so that higher z-scores denote more severity.

Group comparisons of grey matter (GM) volumes for each region of 94 anatomical regions included in the Automated Anatomical Labelling 3 (AAL3) atlas[26] (for the 94 regions, see Supplementary Table 1) were performed by computing T- and p-values using a GLM with total intracranial volume (TIV), age, and the difference between MRI and MEG dates as covariates. Eighty-seven regional GM volumes were significantly smaller in patients with AD than in controls, especially in temporal regions (Supplementary Fig. 1 and Supplementary Table 2). Amongst them, we focused on a volume of the parahippocampal gyrus (PHG) as a key indicator of neurodegeneration in AD progression. The PHG includes perirhinal and entorhinal cortices of the medial temporal lobe (MTL), and MRI-based studies have reported that the volume of MTL reduces, especially in the perirhinal and entorhinal cortices, in the early stages of typical AD[27–29]. PHG volume was defined as a summation of the volumes of left- and right-hemisphere PHGs. The average PHG volume in patients with AD was 7.99 ml ± 0.09, and the average PHG in the controls was 9.28 ml ± 0.11 [$t(143) = -9.508$; $p < 0.001$; see also Fig 1a]. The PHG volumes for each subject were adjusted for covariates of TIV, age, and the difference between MRI and MEG dates using a GLM. We also defined PHG volume loss z-scores, z_{PHG} (Fig. 1b), standardized by the adjusted PHG volumes of the control group and sign-inverted so that higher z-scores denote more severity.

Abnormal frequency specific long-range and local neural synchrony in AD

We computed six scalar metrics to quantify long-range (amplitude envelop correlation, AEC) and local synchrony (spectral power): [i] frontal delta-theta-band AEC, [ii] whole-brain alpha-band AEC, [iii] whole-brain beta-band AEC, [iv] whole-brain delta-theta-band spectral power, [v] temporal alpha-band spectral power, and [vi] whole-brain beta-band spectral power (the temporal and frontal regions of interest are depicted in Supplementary Fig. 2). For each scalar metric, we computed the average within several regions where large region-level group differences were identified between patients with AD and controls (Supplementary Fig. 3c–f and Supplementary Tables 3, 4). Specifically, for the regional AECs, a significant increase in delta-theta-band AEC in patients with AD was identified in frontal regions, and significant reductions in alpha- and beta-band AECs in patients with AD were identified in the whole brain. For the regional spectral power, delta-theta-band power in patients with AD was increased in the whole brain, and significant reductions in alpha- and beta-band power in patients with AD were identified in

temporal regions and the whole brain, respectively. The observed regional contrasts in delta-theta- and beta-band AECs were similar to those seen between AD dementia and subjective cognitive decline (SCD) in an MEG study[17], though in that study the changes in alpha band in AD-dementia group were observed only in temporal regions. An EEG study[30], however, has reported that alpha-band AEC decreases in AD dementia compared to SCD in almost the whole brain, which is consistent with our result. For the spectral power, the regional contrasts were similar to those seen between MCI and controls in an MEG multi-center study[14].

In line with the region-level comparisons, scalar metrics of long-range and local neural synchrony in delta-theta band were increased in patients with AD compared to controls. In contrast, scalar metrics of long-range and local and synchrony in alpha and beta bands were reduced in patients with AD compared to controls (Supplementary Fig. 3a, b). We performed z-scoring for each scalar metric, z_{MEG}, based on age-adjusted values, standardizing them by the values of the control group. For the alpha- and beta-band metrics, raw z-score values were negative in patients with AD, and we multiplied the values by -1 so that higher z-scores denote more severity consistently.

PHG volume loss precedes MMSE decline in Atrophy-Cognition-EBM staging of AD progression

An AC-EBM analysis with the two metrics, PHG volume loss, z_{PHG}, and MMSE decline, z_{MMSE}, was performed for six events (i.e., $N = 6$; three events for each metric). Robust event thresholds were determined by exhaustive search of multiple event thresholds and choosing the set of event thresholds that maximized the EBM likelihood (Supplementary Fig. 4, Step 2). The AC-EBM provided seven stages, each located between consecutive event occurrence times. Based on the probabilities that each subject is assigned to each of the seven stages, the ratio of subjects categorized to each stage was computed (Fig. 1e). The ratio of subjects with CDR 0.5 was largest in stage 4, and the ratio of controls (CDR$=0$) in stage 4 was small compared with those at less severe stages of 1–3, indicating that stage 4 best corresponds to clinical MCI due to AD.

Trajectories of PHG volume loss and MMSE scores were computed as probability-based weighted means [Fig. 1g; see also equation (4) in Methods]; the trajectory of PHG volume loss preceded that of MMSE decline, consistent with the relationship between brain atrophy and cognitive decline described in a hypothetical model of biomarker trajectories[2,3]. Figure 1f shows the distribution of the seven stages in the PHG volume loss versus MMSE score space, which was obtained by distinctly allocating each subject to one of the stages with maximum probability. The dot colors denote the seven stages. A star symbol denotes weighted means for stage 4: z_{PHG} of 1.33 ± 0.258 (mean$\pm$SE) and MMSE score of 26.3 ± 0.82 (mean$\pm$SE). The value of z_{PHG} was in the range of 1–2. The value range is used to represent a mild-atrophy range in the voxel-based specific regional analysis system for Alzheimer's disease (VSRAD) software[31,32] that has been used as a diagnostic tool to detect early stages of AD.

Moreover, the MMSE score of 26.3 is in the range of 23–27, which is considered to be typical for MCI due to AD[33,34]. Stage 4 therefore corresponds to MCI stage, whereas stages 3 and 5 may correspond to preclinical-AD and mild-AD-dementia stages, respectively.

Grey-matter-volume z-scores as a function of the seven stages were also computed (Fig. 1h; equation (4) in Methods). The evolution of brain atrophy approximated typical AD progression reported in MRI-based studies; GM volume loss in AD starts in the MTL in MCI stage, spreads to lateral temporal and parietal lobes in mild-AD-dementia stage, and spreads further to frontal lobe in moderate-AD-dementia[35–37]. In our data (Fig. 1h), prominent atrophy with $z > 1$ was observed over most of the temporal regions starting at stage 4 that might correspond to MCI stage (the GM-atrophy spatial pattern was circled with a dotted line in Fig. 1h).

These AC-EBM results indicate that PHG volume loss precedes MMSE decline, and they track the stages of AD from preclinical AD to moderate-AD-dementia. The event order of GM volume loss and cognitive decline is consistent with the observation that cognitive decline in the early stage of AD progression reflects neuronal loss in medial temporal regions[1,4].

Neural synchrony progressively changes across AD stages estimated by Atrophy-Cognition-EBM

[Figure 2 about here.]

For each of the seven AD stages determined by the AC-EBM analysis (Fig. 1e–h), profiles of neural synchrony were estimated by computing probability-based weighted means of long-range and local synchrony [equation (4) in Methods] corresponding to each stage (Fig. 2). Along the AD stages, delta-theta-band synchrony consistently increased, and alpha- and beta-band synchrony consistently decreased, respectively. Consistent with the finding that stage 4 corresponds to the clinical stage of MCI due to AD, neural synchrony showed prominent changes around stage 4. Alpha- and beta-band long-range synchrony decreased steadily across stages 1–3 and then decreased further in stage 4 (Fig. 2a). Beta-band local synchrony also decreased by half from 1 to 4 (Fig. 2b). In contrast, there were little changes in delta-theta-band long-range synchrony and delta-theta- and alpha-band local synchrony from stage 1 to 3 but these changes became prominent after stage 3.

Regional patterns of long-range and local synchrony as a function of the seven stages were computed as the deviations from the mean regional patterns of the controls, i.e., the z-scores standardized by the controls (Fig. 2c, d). Prominent deviations in these metrics manifested at stage 4 (Fig. 2e, f; the top 10 regions with significant differences were shown in Supplementary Tables 5 and 6, respectively). The regions with prominent deviations overlapped with the regions where significant increase/decrease in the neural synchrony were seen in group comparisons (see Supplementary Fig. 3e, f).

The changing patterns with AD progression indicate that neural synchrony are sensitive indicators of functional change along the AD progression. To further examine the temporal association of functional deficits to neurodegeneration and cognitive decline, we included neural synchrony in addition to the PHG volume loss and MMSE decline (Synchrony-Atrophy-Cognition-EBM, SAC-EBM).

Long-range synchrony changes in alpha and beta bands precede PHG volume loss and MMSE decline

[Figure 3 about here.]

SAC-EBM analyses that included PHG volume loss, z_{PHG}, MMSE decline, z_{MMSE}, and neural synchrony metric z-scores, z_{MEG}, were performed for nine events (i.e., $N = 9$; three events for each metric). Separate SAC-EBMs were performed for delta-theta-, alpha-, and beta-band long-range neural synchrony metrics. Each EBM determined the order of nine events, thus defining ten stages between consecutive event occurrence times (Supplementary Fig. 5). The probabilities that each subject is assigned to each of the ten stages were also computed, and the ratio of subjects categorized to each stage was evaluated (Fig. 3a, e, i). Based on the probabilities, trajectories of long-range synchrony, of PHG volume loss, and of MMSE score change were computed as their probability-based weighted means (Fig. 3b, f, j). Regional profiles of the long-range synchrony as a function of the ten stages were also computed as probability-based weighted means of the z-scores (not sign-inverted ones) standardized by the controls (Fig. 3c, g, k).

For all frequency bands, around stages 5 and 6, the weighted means of PHG volume loss z-scores were in the range of 1–2 and the MMSE scores were in the range of 23–27. Moreover, the ratio of the subjects with CDR$= 0.5$ was largest at stage 5. These indicated that stage 5 best represents the onset of clinical MCI stage and stages 1-4, where MMSE scores remain almost constant at or near 30, correspond to the preclinical stages of AD. The changes in long-range synchrony during the preclinical stages are shown as statistical bars, and the corresponding region-level changes are shown in Figures 3d, h, and l.

Alpha- and beta-band long-range synchrony robustly decreased during the preclinical stages of AD, preceding both PHG volume loss and MMSE decline. Specifically, between stages 1 and 4, the alpha- and beta-band long-range synchrony decreased by more than 80 % of the total drop seen from stage 1 to 10. Whole-brain regions, but especially temporal regions, were involved in these prominent preclinical changes (Fig. 3h, l; the top 10 regions with significant differences were listed in Supplementary Table 8).

In contrast, the trajectory of delta-theta-band long-range synchrony (Fig. 3b, c) was paralleled or lagged the evolution of PHG volume loss across almost all the stages, but a large variation occurred around the MCI stages

(stages 5 and 6) as was seen with the AC-EBM analysis (Fig. 2b). A comparison of regional patterns seen in stages 5 and 1 indicated that there were no significant increases (Fig. 3d), which was consistent with an observation seen in the AC-EBM analysis (Fig. 2f).

Trajectory shapes of PHG volume loss (almost linear) and MMSE scores (half-parabola) were similar to those obtained in the AC-EBM analysis (Fig. 1g), indicating that the SAC-EBM staging including long-range synchrony describes almost the same AD progression as the AC-EBM staging. This further indicates that prominent changes in alpha- and beta-band long-range synchrony during preclinical stages can be utilized to stratify the preclinical stages determined only by neurodegeneration and cognitive deficits.

Local synchrony changes in alpha and beta bands precede PHG volume loss and MMSE decline

[Figure 4 about here.]

SAC-EBM analyses for PHG volume loss, z_{PHG}, MMSE decline, z_{MMSE}, and local neural synchrony metric z-scores, z_{MEG}, were performed for nine events (i.e., $N = 9$; three events for each metric). Separate SAC-EBMs for delta-theta-, alpha-, and beta-band spectral power metrics were performed. Similar to findings with long-range synchrony, the SAC-EBMs determined the order of nine events and ten stages (Supplementary Fig. 5). The probabilities that each subject is assigned to each of the ten stages were computed, and the ratio of subjects categorized to each stage was evaluated (Fig. 4a, e, i). Based on the probabilities, trajectories of local synchrony, of PHG volume loss, and of MMSE score change were computed (Fig. 4b, f, j). Regional profiles of the local synchrony were also computed as probability-based weighted means of the z-scores (Fig. 4c, g, k). When considering delta-theta- and alpha bands, around stages 6 and 7, the weighted means of PHG volume loss z-scores were in the range of 1–2 and the MMSE scores were in the range of 23–27, indicating that stage 6 best represents the onset of the MCI stage clinically. Moreover, the ratios of the subjects with CDR$= 0.5$ were large at stages 6 and 7. For beta band, stage 6 best represented the MCI stage. For all frequency bands, stages 1-5, where MMSE scores remain almost constant at or near 30, corresponded to the preclinical stages of AD. The changes in local synchrony during the preclinical stages are shown as statistical bars, and the corresponding region-level changes are shown in Figures 4d, h, and l (the top 10 regions with significant differences were listed in Supplementary Table 10).

Alpha- and beta-band local synchrony decreased during the preclinical stages of AD, preceding both PHG volume loss and MMSE decline (Fig. 4f, g, j, k), while delta-theta-band local synchrony increased lagging the evolution of PHG volume loss especially in the preclinical stages (Fig. 4b, c). Specifically, alpha-band local synchrony decreased considerably by the onset of the MCI stage. A comparison of regional patterns during the preclinical stages (stages 6 vs 1) showed that there were significant alpha-band local synchrony reductions in temporal regions (Fig. 4h), similar

to the regional contrasts observed in the group comparison (Supplementary Fig. 3e). It is noted that these trends were inconsistent with those found in the AC-EBM analysis (Fig. 2a), especially within the phase of the preclinical stages, where there was little change found in the alpha-band local synchrony. This can be interpreted as evidence that early stages in AD progression can be better characterized by including neurophysiological markers as AD indicators. Beta-band local synchrony also decreased largely during preclinical stages, preceding PHG volume loss and MMSE decline; by stage 5, the whole-brain beta-band power decreased by approximately 55 % of the total drop seen from stage 1 to 10. Moreover, the change during preclinical AD stages occurred in the whole brain (Fig. 4l), similar to the regional contrasts observed in the group comparison (Supplementary Fig. 3e). In contrast to alpha- and beta-band local synchrony, delta-theta-band local synchrony increased lagging the evolution of PHG volume loss in the preclinical stages and made a large jump around stages 6 and 7. The jump was supported by comparing regional patterns between stages 6 and 1 (Fig. 4d). The *hyper*-synchrony spatial pattern was similar to that observed in the group comparison between AD and controls (Supplementary Fig. 3e).

As shown in the previous section, large alpha- and beta-band *hypo*-synchrony during the preclinical stages were also seen in the long-range synchrony (Fig. 3f, j). Notably, the decreases in the long-range metrics were much greater than those in the local metrics, especially in the early stages during the phase of the preclinical AD (i.e., around stages 1–3).

Discussion

In this study we demonstrate that functional deficits of frequency-specific neural synchrony show progressive changes across AD stages and that synchrony changes occur at the earliest stages of AD preceding neurodegeneration and cognitive decline. Specifically, both long-range and local neural synchrony, in the alpha and beta bands but not in the delta-theta band, were found to decrease in preclinical stages of AD, preceding both PHG atrophy and MMSE decline, with more robust findings for long-range neural synchrony. These findings highlight the frequency-specific manifestations of neural synchrony in AD and that synchrony reductions in alpha and beta bands are sensitive indices reflecting functional deficits in the earliest stages of disease progression. We first discuss the implications of three key findings: 1) electrophysiological assays of neural synchrony precede volume loss and cognitive decline, 2) frequency-specific manifestations of neural synchrony deficits along disease progression, and 3) distinction between long-range and local synchrony deficits in disease progression.

Functional deficits as depicted by reduced neural synchrony precede structural volume loss and cognitive deficits. The EBM algorithms on cross-sectional multimodal imaging data clearly demonstrated that alpha- and beta-band synchrony within inferior temporal and posterior parieto-occipital regions show significant deficits in the early

disease stages–stages where volumetric and clinical deficits are still not significantly deviated from their baseline trajectory. This is consistent with the finding that functional changes occur earlier in the time course than structural changes in AD[2,3].

Previous functional MRI studies have demonstrated disrupted connectivity especially between the hippocampus and several cortical default mode network (DMN) areas in subjects with amyloid deposition but without cognitive impairment[38]. Such a disruption in the default network have also observed in clinically normal older individuals without prominent brain atrophy in MTL preserving hippocampal activity[39,40], indicating altered functional connectivity during the period of preclinical AD. In contrast to fMRI data that reflects the cascade of neural, metabolic, hemodynamic events in AD, the current study findings from MEG, which captures the synaptic physiology in the collective oscillatory spectra, demonstrates direct AD-related altered neuronal activity preceding both neurodegeneration and cognitive decline.

The current study further demonstrated that the oscillatory deficits and their temporal association to neurodegeneration and cognitive decline are frequency specific. In particular it is alpha and beta hyposynchrony that precede PHG atrophy and MMSE decline, while delta-theta hypersynchrony does not seem to show such precedence. This is consistent with previous findings from our group as well as others that alpha and beta hyposynchrony is more tightly associated with tau accumulation which is closely allied to neurodegeneration and cognitive decline in AD[15,41,42]. Neural hyposynchrony in alpha and beta bands that precede in timeline may therefore represent harbingers of altered synaptic physiology associated with tau accumulation in AD. Indeed, in human postmortem studies, the strongest correlate of cognitive deficits in patients with AD is synapse loss[43,44]. Basic science studies using transgenic AD mice have also shown that synaptotoxicity is an early phenomenon in AD pathophysiology[45]. In the context of fluid biomarkers to detect the presence of plasma amyloid in cognitively-unimpaired individuals, alpha and beta neural hyposynchrony can detect and quantify tau associated neurodegenerative mechanisms and hence may provide crucial information for early therapeutic interventions.

Previous studies have also shown that delta-theta oscillatory activity is increased in AD and is strongly associated with amyloid accumulation[15,46]. In particular, increased delta-theta activity is a robust signal in individuals who are amyloid positive and cognitively unimpaired as well as those who harbor APOE-ε4 allele and an increased risk of AD[13,47]. These findings indicate that delta-theta hypersynchrony is an early change in AD spectrum and may even precede the neurodegeneration and cognitive deficits changes. However, in the current results, the trajectory of delta-theta hypersynchrony was either identical or lagged that of PHG volume loss. This apparent controversy may be because of the region-specific effects of delta-theta hypersynchrony in early versus late AD. For example,

hypersynchrony in early AD is more localized to lateral and dorsomedial frontal cortices and evolves into the whole brain with disease progression. Although we considered the region-specific synchrony metrics (e.g., frontal delta-theta-band AEC) into the EBM analysis defining the region of interests based on the group contrasts, the focused regions might have been ineffective to sensitively describe early delta-theta changes. It is also noteworthy that delta-theta oscillatory changes are more closely allied to amyloid accumulations in AD, which become saturated early in the disease course and have poor association with the neurodegeneration and cognitive trajectories in AD. It is worthy of future analyses to explore how the trajectory of early-saturated variables may be captured by the EBM models.

The decrease in the alpha- and beta-bands long-range metrics in the preclinical stages was much greater than that in the local metrics. This is consistent with the fact that AD-related abnormal brain activities are observed as disruptions of functional networks. Long-range cross-regional metrics, such as AECs, directly capture such network disruptions involving all brain regions while the local metrics capture features of individual regions. From the definition, local synchrony describes neuronal collective oscillations in each local region and thus the change along AD progression may depend on long-term, slowly changing neuronal loss. On the other hand, long-range synchrony describes temporal coherence amongst the regional collective oscillations and is vulnerable to altered neuronal oscillations along AD progression. Long-range metrics are therefore more sensitive to abnormal rhythms, gathering local abnormalities.

Preclinical neurophysiological markers indicating AD pathophysiology are clinically important but have not been established. Aβ accumulation in preclinical stages is just a necessary condition for AD, and additional preclinical markers are required to fully predict AD progression. From this point of view, the present study indicates that alpha- and beta-band MEG metrics, especially long-range-synchrony metrics (AEC), which were found to be sensitive to preclinical stages, might be promising candidates as such additional markers. According to an MEG study on the reproducibility of functional connectivity changes in AD[17], beta-band AEC has been reported to be more robust than alpha-band AEC. Considering the reproducibility results shown in the MEG study, beta-band AEC is the most robust preclinical AD marker amongst the neural synchrony metrics we considered in this study.

A limitation of the current study is that there were differences in age between controls and patients with AD. Although we performed age adjustments for each metric by employing GLMs, it has been reported that age trajectories in neurophysiological measures are not linear even in healthy ageing[48]. It has also been reported that age-related changes in brain atrophy follow a nonlinear time course depending on the brain areas[49]. These studies indicate that it may be better to employ a nonlinear method beyond GLMs to perfectly correct ageing effects.

Although we clarify for the first time the time courses of MEG neurophysiological metrics in AD progression in this study, another limitation is that we have not examined the heterogeneity in AD progression. Indeed, AD is a heterogeneous, multifactorial disorder with various pathobiological subtypes[50]. In this context, an EBM called *Subtype and Stage Inference* (SuStaIn)[21] capable of capturing both spatial and temporal heterogeneity of diseases has been applied to subtyping of neurodegenerative diseases including typical AD. The SuStaIn has also been applied to find different spatio-temporal trajectories of longitudinal tau PET data in AD[51]. Since oscillatory rhythms are thought to depend on AD subtypes[18,52], an extended trajectory analysis considering both spatial and temporal variations of MEG/EEG metrics is warranted in the future and such analyses could be used to examine distinct neurophysiological trajectories depending on AD subtypes.

Methods

Participants

We studied 78 patients who met National Institute of Aging–Alzheimer's Association (NIA-AA) criteria for probable Alzheimer's disease or MCI due to AD[4,53,54], and 70 cognitively-unimpaired older adults. Clinical diagnosis for patients with AD was established by consensus at a multidisciplinary team; 67 of the 78 patients were confirmed with positive AD biomarkers. The cognitively normal controls were recruited from the community and the eligibility criteria that included normal cognitive performance, normal MRI, absence of neurological, psychiatric, or other major medical illnesses. All participants were recruited from research cohorts at the University of California San Francisco Alzheimer's Disease Research Center (UCSF-ADRC). Neuropsychological assessment for each participant was performed via MMSE within an average of 0.48 years (range: −2.83–1.50) and 0.22 years (range: −1.52–1.01) of the MEG evaluation for controls and patients, respectively. A structured caregiver-interview was used to assess the CDR scales in each participant. Informed consent was obtained from all participants or their assigned surrogate decision makers. The study was approved by the UCSF Institutional Review Board.

MRI acquisition and analyses

Structural brain images were acquired using a unified MRI protocol on 3T Siemens MRI scanners (MAGNETOM Prisma or 3T TIM Trio) at the Neuroscience Imaging Center (NIC) at UCSF, within an average of 1.05 years (range: −6.91–0.78) and 0.29 years (range: −2.13–1.29) of the MEG evaluation for controls and patients, respectively. Structural MRIs were used to generate the head model for source reconstructions of MEG sensor data and to evaluate GM volumes. Region-based GM volumes corresponding to 94 anatomical regions included in the AAL3 atlas (label numbers: 1–94)[26] were computed using the Computational Anatomy Toolbox[55], CAT12 [version 12.8.1 (1987)],

which is an extension of SPM12[56]. GM volumes inside the respective regions were evaluated by the region-based morphometry pipeline implemented in CAT12 with default parameters. Total intracranial volume (TIV), the sum of all segments classified to grey and white matters, and cerebrospinal fluid, was also computed as an output of the pipeline for each subject. The quality of images was estimated by using the automated image quality rating (IQR) implemented in CAT12. As described in an online manual (https://neuro-jena.github.io/cat12-help/), the IQRs range from 0.5 to 10.5; values around 1 and 2 describe (very) good image quality (grade A and B), and values around 5 (grade E) and higher (grade F) indicate problematic images. Our MRIs had a mean IQR value of 2.70 (range: 2.37–3.56) with good (B-) to sufficient (D+) ratings; most of images (87.8 %) were in satisfactory (C) rating, and one image had the D+ rating. Our MRI quality was therefore comparable to that of typical clinical data that is expected to get good to satisfactory ratings.

Resting-state MEG

Data acquisition

Each participant underwent 10–60-minutes resting-state MEG at the UCSF Biomagnetic Imaging Laboratory. The MEG was recorded with a 275-channel whole-head CTF Omega 2000 system (CTF MEG International Services LP, Coquitlam, British Columbia, Canada). Three fiducial coils including nasion and left and right pre-auricular points were placed to localize the position of head relative to sensor array, and later co-registered to individual MRI to generate an individualized head shape. Data collection was optimized to minimize within-session head movements and to keep it below 0.5 cm. For analysis, a 10-min continuous recording was selected from each subject while lying supine and awake with eyes closed (sampling rate $f_s = 600$ Hz). From the continuous recordings, we further selected a 1-min continuous segment with minimal artefacts (i.e., minimal excessive scatter at signal amplitude) for each subject.

Pre-processing

Each 1-min sensor signal was digitally filtered using a bandpass filter of 0.5–55 Hz. Power spectral density (PSD) of each sensor signal was computed, and artefacts were confirmed by visual inspection; channels with excessive noise within individual subjects were removed prior to the following process. When environmental noises larger than a few pT/Hz$^{1/2}$ were observed in a PSD, the dual signal subspace projection (DSSP)[57,58] with the lead-field vectors computed for each individual subject's head model was applied to the filtered sensor signal for the removal of them. As a parameter, we chose the dimension of pseudo-signal subspace as $\mu = 50$. The DSSPs were needed to be applied to thirteen of total 148 subject's signals. For the thirteen data, the resulting dimension of spatio-temporal intersection, i.e., the degree of freedom to be removed, was 3 or 4. We also applied a preconditioned independent

component analysis (ICA)[59] to the signal to identify cardiac components and remove them for all subjects' sensor signals. In each data, one or two clear cardiac ICA-component waveforms with approximately 1-Hz rhythms were observed, which were easily identified by visual inspections.

Atlas-based source reconstruction

Isotropic voxels (5 mm) were generated in a brain region of a template MRI, resulting in 14,125 voxels inside a brain. The generated voxels were spatially normalized into individual MRI space, and subject specific magnetic lead-field vectors were computed for each voxel using a single-shell-model approximation[60]. The voxels for each subject were indexed to the 94 cortical/sub-cortical regions included in the AAL3 atlas[26].

Array-gain scalar beamformer[61] was applied to the 60-sec cleaned sensor time series to obtain voxel-level source-localized activities, i.e., voxel time courses. Lead-field vectors were normalized to avoid the center-of-the-head artifact and a generalized eigenvalue problem was solved to determine the optimum source orientation[62]. The beamformer weights were calculated in the time domain; a data covariance matrix was computed using a whole 60-sec time series, and a singular value truncation (threshold of $10^{-6} \times$ maximum singular value) was performed when inverting the covariance matrix. Ninety-four regional time courses were extracted with alignment to the AAL3 atlas by performing principal component analysis (PCA) across voxel-level time courses within a region and taking a time course of the first principal component. The pre-processing and source reconstructions described above were performed using in-house Matlab scripts utilizing Fieldtrip toolbox functions[63]. We also used BrainNet Viewer toolbox[64] to obtain brain rendering images of MEG metrics and GM atrophy.

MEG resting-state metrics

Based on the 94 regional time courses derived from MEG, we evaluated two measures of neural synchrony: the amplitude-envelope correlation (AEC) and spectral power, which describe long-range and local neural synchrony, respectively. Three canonical frequency bands were considered: 2–7 Hz (delta-theta), 8–12 Hz (alpha), and 15–29 Hz (beta) bands. In Supplementary Fig. 6, the canonical frequency bands were visualized with normalized PSDs averaged across the whole brain for controls and patients with AD, respectively. In terms of the average PSD in AD, a clear alpha peak disappeared, which has been consistently observed in neurophysiological studies[65]. Alpha frequencies at each region in patients with AD generally decrease (i.e., alpha slowing) compared with controls, and the magnitude of alpha slowing depends on brain regions as well as subjects; for example, alpha slowing is prominent in temporal regions. Averaging over PSD curves with different alpha peaks therefore results in disappearance of an alpha peak in the average PSD for AD.

The AECs for a given band is defined as Pearson's correlations between any two envelopes of regional time

courses (total $94 \times 93/2 = 4,371$ pairs). Regional time courses were first processed by a band-pass filtering for a given band, and then their envelopes were extracted by Hilbert transform. To discount spurious correlations caused by source leakages, we orthogonalized any two band-limited time courses before computing their envelopes by employing a pairwise orthogonalization method[66,67]. The AEC with leakage correction is often expressed as AEC-c and is known as a robust measure[68]. The pairwise orthogonalization method provides asymmetric values between two time courses; the value depends on which time course is taken as a seed. Therefore, the Pearson's correlations between the orthogonalized envelopes for both directions were averaged, resulting in 94×94-symmetric AEC matrix. Regional AECs, which correspond to the node degrees in the context of graph theory, were computed by averaging over row or column components of the symmetrized AEC matrix. Whole-brain AECs were computed by averaging regional AECs across the 94 regions. For delta-theta band, we also introduced a frontal scalar metric that was computed by averaging regional AECs across selected 12 sub-regions in frontal region.

The spectral power of a given band, which has often been used as a metric to discriminate patients with AD from controls[9,65,69], is defined by the ratio of a band power to total power and was computed from regional PSDs. The regional PSDs were computed from the 94 regional time courses using Welch's method (50% overlapping) with a 0.293-Hz $(= f_s/2048)$ step. In addition to the region-level power, a whole-brain band-limited power, which represents a whole-brain mean band power, was computed by averaging regional power across the 94 regions. For alpha band, we also introduced a temporal scalar metric that was computed by averaging regional power across selected 20 sub-regions in temporal region.

Metric trajectory analyses

Event-based sequencing modeling

Imaging and neuropsychological biomarkers for AD are continuous quantities taking from normal to severe values whereas disease stages are discrete quantities that can only be identified by comprehensively estimating the values of biomarkers[3]. As a data-driven disease progression model, an event-based sequencing model (EBM) that allows us to make inferences about disease progression from cross-sectional data has been proposed[19–21]. In an EBM[19], disease progression is described as a series of metric events, where an event is defined as an occurrence of metrics' abnormal value, and the values of events work as thresholds to determine discrete disease stages. The model in turn infers temporal sequences of the events from cross-sectional data. It is also possible to set multiple events per metric by defining them as occurrences of taking certain z-scores within the range from initial to final z-scores, in which z-scores for each metric linearly increase between all consecutive events and stages are located at temporal midpoints between the two consecutive event occurrence times[21]. In this linear z-score event model, a metric trajectory can be

described as a series of metric values evaluated at estimated stages.

We utilized the linear z-score model to quantify metric trajectories, employing a multivariate-Gaussian-form data likelihood:

$$P(Z|S) = \prod_{j=1}^{J} \sum_{k=1}^{N+1} p(\text{stage}(j) = k|S) p(Z_j|S, \text{stage}(j) = k), \tag{1}$$

where a conditional probability, $p(Z_j|S, \text{stage}(j) = k)$, that a subject j takes biomarker values of Z_j given that $\text{stage}(j) = k$ (i.e., the subject j has been in a stage k) and a sequence of events S, is proportional to a Gaussian distribution:

$$p(Z_j|S, \text{stage}(j) = k) \propto \exp\left(-\sum_{i=1}^{I} \frac{(z_{ij} - \mu_i(k))^2}{2}\right). \tag{2}$$

Here N denotes a total number of events, and i, j, and k are indices of metrics, subjects, and stages, respectively. J is the number of subjects ($J = 148$). I is the number of metrics: $I = 2$ for an AC-EBM and $I = 3$ for an SAC-EBM, respectively. The symbol $Z_j = [z_{1j}, z_{2j}, \ldots, z_{Ij}]^{\mathrm{T}}$, where z_{ij} denotes z-score of a metric i for subject j, and the symbol $Z = [Z_1, Z_2, \ldots, Z_J]$ describing the data matrix with $I \times J$-dimension. $\mu_i(k)$ denotes a k-th stage value of a metric i and is given by a linearly interpolated midpoint z-score between two z-scores evaluated at consecutive event occurrence times. Since there are total $N+2$ event occurrence times including the initial and final times, $N+1$ stages are provided. When employing equation (1), we assumed the prior distribution was uniform: $p(\text{stage}(j) = k|S) = (N+1)^{-1}$. A linear z-score model and the relationship between a set of events and the estimated stages are illustrated at the bottom of Step 1 panel of Supplementary Fig. 4.

The most likely order of events is given by the event sequence S that maximizes the posterior distribution $P(S|Z) = P(S)P(Z|S)/P(Z)$. On the assumption that the prior $P(S)$ is uniformly distributed[19], the most likely sequence is obtained by solving the maximum likelihood problem of maximizing equation (1). To solve the problem, for a given set of events, we performed Markov Chain Monte Carlo (MCMC) sampling on sequences[21] and chose the maximum likelihood sequence from $50,000$ MCMC samples.

z-scored metrics

We considered each of the PHG volume, MMSE score, and scalar neural synchrony metrics. Since a linear z-score model, equation (1), assumes a monotonous increase in z-scored metrics along disease progression, i.e., higher stage denotes more severity, "sign-inverted" z-scores were introduced to the metrics with decreasing trends along disease progression. Specifically, for GM volumes, MMSE score, and alpha- and beta-band neural synchrony

metrics, the z-score of a metric i for a subject j was defined by $z_{ij} = (\bar{x}_i^{\mathrm{C}} - x_{ij})/\sigma_i^{\mathrm{C}}$, where x_{ij} denotes a value of a metric i for a subject j, and $\bar{x}_i^{\mathrm{C}}$ and σ_i^{C} denote the mean and standard deviation (SD) of the controls' metric values, respectively. For delta-theta-band neural synchrony metrics, z-scores were defined in a standard way as $z_{ij} = (x_{ij} - \bar{x}_i^{\mathrm{C}})/\sigma_i^{\mathrm{C}}$. Using these z-scored metrics, the initial and final events, z_{initial} and z_{final}, for each metric were set as the bottom and top 10% average z-scores, respectively. The initial and final z-scores we used in AC- and SAC-EBMs were: $(z_{\mathrm{initial}}, z_{\mathrm{final}}) = (-1.372, 3.804)$ for PHG volume loss z-score and $(-0.902, 12.712)$ for MMSE-decline z-score, respectively; $(z_{\mathrm{initial}}, z_{\mathrm{final}}) = (-1.083, 2.811)$, $(-1.542, 1.605)$, and $(-1.624, 1.641)$ for the delta-theta-, alpha-, and beta-band long-range synchrony, respectively; $(z_{\mathrm{initial}}, z_{\mathrm{final}}) = (-1.329, 6.097)$, $(-1.461, 2.866)$, and $(-1.810, 2.784)$ for the delta-theta-, alpha-, and beta-band local synchrony, respectively.

Events-setting optimization

In addition to the initial and final z-score events, z_{initial} and z_{final}, we set three events for each metric because various possible curves of metric trajectories were supposed to be expressed by three variable points with the two fixed points. For example, in an AC-EBM analysis, i.e., a two-metric trajectory analysis for PHG volume loss and MMSE decline, total six events were set $(N = 6)$. The metric trajectory as a series of stage values, $\mu_i(k)$, is sensitive to event settings because pre-defined events do not necessarily capture appropriate boundaries between disease stages. To determine disease stages less sensitive to the specification of the z-score events, we tried several sets of events and selected the set of events with the largest data likelihood amongst the trials. Specifically, we searched the set of events better fitting the data Z by choosing three z-scores from $\{0.2, 0.3, 0.4, 0.5, 0.6, 0.7, 0.8\}$-quantiles for each metric, and thus the number of event combinations for each metric was $({}_7C_3 =)35$. The MCMC samplings ($50,000$ samples for each set of events) were accordingly performed $1,225$ times for an AC-EBM and $42,875$ times for an SAC-EBM, respectively, to find the set of events and their sequence $\bar{S}$ with the largest data likelihood. This exhaustive search of event settings, which was not implemented in a conventional linear z-score model[21], is diagrammatically shown in Supplementary Fig. 4.

Trajectory computations

Given the most likely sequence $\bar{S}$ as the results of the exhaustive search, the probabilities that a subject j falls into a stage k are evaluated by the posterior distribution

$$p(\mathrm{stage}(j) = k | Z_j, \bar{S}) = \frac{p(Z_j | \bar{S}, \mathrm{stage}(j) = k)}{\sum_{k'} p(Z_j | \bar{S}, \mathrm{stage}(j) = k')}. \tag{3}$$

The probabilities $p_j(k) \equiv p(\text{stage}(j) = k | Z_j, \bar{S})$ can be viewed as the contribution of a subject j to a stage k, which allows us to evaluate a stage value of a metric i at a stage k as a weighted mean with the probabilities:

$$\bar{x}_i(k) = \frac{p_1(k) \cdot x_{i1} + p_2(k) \cdot x_{i2} + \cdots + p_J(k) \cdot x_{iJ}}{p_1(k) + p_2(k) + \cdots + p_J(k)}. \tag{4}$$

Then, we represented the trajectory of the metric i by a series of the stage values, $\bar{x}_i(k)$. The standard error (SE) of the weighted mean at a stage k was evaluated by

$$\text{SE}(k) = \sigma_i \cdot \left[\frac{p_1(k)^2 + p_2(k)^2 + \cdots + p_J(k)^2}{(p_1(k) + p_2(k) + \cdots + p_J(k))^2} \right]^{1/2}, \tag{5}$$

where σ_i is a standard deviation of a metric i. This definition of SE provides an usual expression of the standard error of the mean, $\sigma_i/\sqrt{J}$, if all subjects equally contributed to the stage k.

These formulations of trajectories were applied to several metrics. In the AC-EBM, the metrics i denote the PHG volume loss z-score or MMSE scores. In the SAC-EBMs, they denote each scalar neural synchrony metric in addition to the PHG volume loss z-score and MMSE score. We also applied them to regional neural synchrony z-scored metrics and GM volume loss z-scores. Moreover, when evaluating the ratio of subjects categorized to each stage (e.g., Fig. 1e), we treated $(x_{i1}, x_{i2}, \ldots, x_{iJ})$ as an one-hot vector, where a metric i represents a subjects' category provided by CDR scale. For example, when evaluating the ratio of subject with CDR$= 0.5$, $x_{ij} = 1$ only when a subject j has CDR scale of 0.5, otherwise $x_{ij} = 0$.

Statistical analysis

To test demographic differences between patients with AD and controls, unpaired t-test was used for age and χ-square tests was used for gender. Age was defined at the time of the MEG scan date. In the statistical analyses, p values below 0.05 were considered statistically significant. For group comparisons of GM volumes, MMSE scores, and neural synchrony metrics, two-sided significance tests (against a null value of zero) were performed using the GLM. For GM volumes, TIV, age, and the difference between MRI and MEG dates were included as covariates. For MMSE scores, age and the difference between MMSE and MEG dates were included as covariates. For neural synchrony metrics, age was included as a covariate. The problem of the multiple comparisons across 94 regions were solved by controlling the Benjamini-Hochberg false discovery rate (FDR)[70]. The FDR-adjusted p-value (i.e., q-value) below 0.05 or 0.01 was considered statistically significant.

A non-parametric test was performed to statistically compare metrics between stages, i.e., to test statistical significance of the difference between stage values represented by weighted means [e.g., stage k vs. k': $\delta x =$

$\bar{x}_i(k) - \bar{x}_i(k')$]. For a metric i, we employed a bootstrap re-sampling (50,000 samples) of an original data set, $\boldsymbol{x}_i = (x_{i1}, x_{i2}, \ldots, x_{iJ})$, to generate new data sets, $(x^\star_{i1}, x^\star_{i2}, \ldots, x^\star_{iJ})$, using a random number generator, where each $x^\star_{ij}$ is one of the components in the original data set $\boldsymbol{x}_i$. We then computed weighted means $\bar{x}^\star_i(k)$ [equation (4)] for each sample. The same procedures were performed for a stage k', obtaining weighted means $\bar{x}^\star_i(k')$ for each sample. We then tested the null hypothesis that a weighted mean at the stage k, $\bar{x}_i(k)$, is equal to a weighted mean at the stage k', $\bar{x}_i(k')$, evaluating p-value generating null distribution of $\delta x^\star = \bar{x}^\star_i(k) - \bar{x}^\star_i(k')$. The problem of multiple comparisons across stages were solved by controlling the FDR. The q-value below 0.05 was considered statistically significant.

References

1. DeTure, M. A. & Dickson, D. W. The neuropathological diagnosis of alzheimer's disease. *Mol. neurodegeneration* **14**, 1–18 (2019).

2. Jack Jr, C. R. *et al.* Brain beta-amyloid measures and magnetic resonance imaging atrophy both predict time-to-progression from mild cognitive impairment to alzheimer's disease. *Brain* **133**, 3336–3348 (2010).

3. Sperling, R. A. *et al.* Toward defining the preclinical stages of alzheimer's disease: Recommendations from the national institute on aging-alzheimer's association workgroups on diagnostic guidelines for alzheimer's disease. *Alzheimer's & dementia* **7**, 280–292 (2011).

4. Jack Jr, C. R. *et al.* Nia-aa research framework: toward a biological definition of alzheimer's disease. *Alzheimer's & Dementia* **14**, 535–562 (2018).

5. Busche, M. A. *et al.* Clusters of hyperactive neurons near amyloid plaques in a mouse model of alzheimer's disease. *Science* **321**, 1686–1689 (2008).

6. Ahnaou, A. *et al.* Emergence of early alterations in network oscillations and functional connectivity in a tau seeding mouse model of alzheimer's disease pathology. *Sci. reports* **7**, 1–14 (2017).

7. Busche, M. A. *et al.* Tau impairs neural circuits, dominating amyloid-β effects, in alzheimer models in vivo. *Nat. neuroscience* **22**, 57–64 (2019).

8. Dubois, B. *et al.* Preclinical alzheimer's disease: definition, natural history, and diagnostic criteria. *Alzheimer's & Dementia* **12**, 292–323 (2016).

9. Jeong, J. Eeg dynamics in patients with alzheimer's disease. *Clin. neurophysiology* **115**, 1490–1505 (2004).

10. Fernández, A. *et al.* Meg spectral profile in alzheimer's disease and mild cognitive impairment. *Clin. Neurophysiol.* **117**, 306–314 (2006).

11. Stam, C. J. *et al.* Magnetoencephalographic evaluation of resting-state functional connectivity in alzheimer's disease. *Neuroimage* **32**, 1335–1344 (2006).

12. Koelewijn, L. *et al.* Alzheimer's disease disrupts alpha and beta-band resting-state oscillatory network connectivity. *Clin. Neurophysiol.* **128**, 2347–2357 (2017).

13. Nakamura, A. *et al.* Electromagnetic signatures of the preclinical and prodromal stages of alzheimer's disease. *Brain* **141**, 1470–1485 (2018).

14. Hughes, L. E. *et al.* Biomagnetic biomarkers for dementia: A pilot multicentre study with a recommended methodological framework for magnetoencephalography. *Alzheimer's & Dementia: Diagn. Assess. & Dis. Monit.* **11**, 450–462 (2019).

15. Ranasinghe, K. G. *et al.* Neurophysiological signatures in alzheimer's disease are distinctly associated with tau, amyloid-β accumulation, and cognitive decline. *Sci. translational medicine* **12** (2020).

16. Meghdadi, A. H. *et al.* Resting state eeg biomarkers of cognitive decline associated with alzheimer's disease and mild cognitive impairment. *PloS one* **16**, e0244180 (2021).

17. Schoonhoven, D. N. *et al.* Sensitive and reproducible meg resting-state metrics of functional connectivity in alzheimer's disease. *Alzheimer's research & therapy* **14**, 1–19 (2022).

18. Ranasinghe, K. G. *et al.* Neuronal synchrony abnormalities associated with subclinical epileptiform activity in early-onset alzheimer's disease. *Brain* **145**, 744–753 (2022).

19. Fonteijn, H. M. *et al.* An event-based model for disease progression and its application in familial alzheimer's disease and huntington's disease. *NeuroImage* **60**, 1880–1889 (2012).

20. Young, A. L. *et al.* A data-driven model of biomarker changes in sporadic alzheimer's disease. *Brain* **137**, 2564–2577 (2014).

21. Young, A. L. *et al.* Uncovering the heterogeneity and temporal complexity of neurodegenerative diseases with subtype and stage inference. *Nat. communications* **9**, 1–16 (2018).

22. Wiesman, A. I., Castanheira, J. D. S. & Baillet, S. Stability of spectral estimates in resting-state magnetoencephalography: recommendations for minimal data duration with neuroanatomical specificity. *NeuroImage* 118823 (2021).

23. Colclough, G. L. *et al.* How reliable are meg resting-state connectivity metrics? *Neuroimage* **138**, 284–293 (2016).

24. Selkoe, D. J. Alzheimer's disease is a synaptic failure. *Science* **298**, 789–791 (2002).

25. Spires-Jones, T. L. & Hyman, B. T. The intersection of amyloid beta and tau at synapses in alzheimer's disease. *Neuron* **82**, 756–771 (2014).

26. Rolls, E. T., Huang, C.-C., Lin, C.-P., Feng, J. & Joliot, M. Automated anatomical labelling atlas 3. *Neuroimage* **206**, 116189 (2020).

27. Teipel, S. J. *et al.* Comprehensive dissection of the medial temporal lobe in ad: measurement of hippocampus, amygdala, entorhinal, perirhinal and parahippocampal cortices using mri. *J. neurology* **253**, 794–800 (2006).

28. Echávarri, C. *et al.* Atrophy in the parahippocampal gyrus as an early biomarker of alzheimer's disease. *Brain Struct. Funct.* **215**, 265–271 (2011).

29. Matsuda, H. Mri morphometry in alzheimer's disease. *Ageing research reviews* **30**, 17–24 (2016).

30. Briels, C. T. *et al.* Reproducibility of eeg functional connectivity in alzheimer's disease. *Alzheimer's research & therapy* **12**, 1–14 (2020).

31. Hirata, Y. *et al.* Voxel-based morphometry to discriminate early alzheimer's disease from controls. *Neurosci. letters* **382**, 269–274 (2005).

32. Matsuda, H. *et al.* Automatic voxel-based morphometry of structural mri by spm8 plus diffeomorphic anatomic registration through exponentiated lie algebra improves the diagnosis of probable alzheimer disease. *Am. J. Neuroradiol.* **33**, 1109–1114 (2012).

33. Saxton, J. *et al.* Computer assessment of mild cognitive impairment. *Postgrad. medicine* **121**, 177–185 (2009).

34. Tsoi, K. K., Chan, J. Y., Hirai, H. W., Wong, S. Y. & Kwok, T. C. Cognitive tests to detect dementia: a systematic review and meta-analysis. *JAMA internal medicine* **175**, 1450–1458 (2015).

35. Scahill, R. I., Schott, J. M., Stevens, J. M., Rossor, M. N. & Fox, N. C. Mapping the evolution of regional atrophy in alzheimer's disease: unbiased analysis of fluid-registered serial mri. *Proc. Natl. Acad. Sci.* **99**, 4703–4707 (2002).

36. Tondelli, M. *et al.* Structural mri changes detectable up to ten years before clinical alzheimer's disease. *Neurobiol. aging* **33**, 825–e25 (2012).

37. Jack Jr, C. R. *et al.* Tracking pathophysiological processes in alzheimer's disease: an updated hypothetical model of dynamic biomarkers. *The lancet neurology* **12**, 207–216 (2013).

38. Sperling, R., Mormino, E. & Johnson, K. The evolution of preclinical alzheimer's disease: implications for prevention trials. *Neuron* **84**, 608–622 (2014).

39. Miller, S. L. *et al.* Age-related memory impairment associated with loss of parietal deactivation but preserved hippocampal activation. *Proc. Natl. Acad. Sci.* **105**, 2181–2186 (2008).

40. Hedden, T. *et al.* Disruption of functional connectivity in clinically normal older adults harboring amyloid burden. *J. Neurosci.* **29**, 12686–12694 (2009).

41. Pusil, S. *et al.* Hypersynchronization in mild cognitive impairment: the 'x'model. *Brain* **142**, 3936–3950 (2019).

42. Ranasinghe, K. G. *et al.* Reduced synchrony in alpha oscillations during life predicts post mortem neurofibrillary tangle density in early-onset and atypical alzheimer's disease. *Alzheimer's & Dementia* **17**, 2009–2019 (2021).

43. DeKosky, S. T. & Scheff, S. W. Synapse loss in frontal cortex biopsies in alzheimer's disease: correlation with cognitive severity. *Annals Neurol. Off. J. Am. Neurol. Assoc. Child Neurol. Soc.* **27**, 457–464 (1990).

44. Terry, R. D. *et al.* Physical basis of cognitive alterations in alzheimer's disease: synapse loss is the major correlate of cognitive impairment. *Annals Neurol. Off. J. Am. Neurol. Assoc. Child Neurol. Soc.* **30**, 572–580 (1991).

45. Zhou, L. *et al.* Tau association with synaptic vesicles causes presynaptic dysfunction. *Nat. communications* **8**, 15295 (2017).

46. Ranasinghe, K. G. *et al.* Altered excitatory and inhibitory neuronal subpopulation parameters are distinctly associated with tau and amyloid in alzheimer's disease. *Elife* **11**, e77850 (2022).

47. Cuesta, P. *et al.* Influence of the apoe $\varepsilon 4$ allele and mild cognitive impairment diagnosis in the disruption of the meg resting state functional connectivity in sources space. *J. Alzheimer's Dis.* **44**, 493–505 (2015).

48. Sahoo, B., Pathak, A., Deco, G., Banerjee, A. & Roy, D. Lifespan associated global patterns of coherent neural communication. *Neuroimage* **216**, 116824 (2020).

49. Coupé, P., Manjón, J. V., Lanuza, E. & Catheline, G. Lifespan changes of the human brain in alzheimer's disease. *Sci. reports* **9**, 1–12 (2019).

50. Jellinger, K. A. Recent update on the heterogeneity of the alzheimer's disease spectrum. *J. Neural Transm.* **129**, 1–24 (2022).

51. Vogel, J. W. *et al.* Four distinct trajectories of tau deposition identified in alzheimer's disease. *Nat. medicine* **27**, 871–881 (2021).

52. Ranasinghe, K. G. *et al.* Distinct spatiotemporal patterns of neuronal functional connectivity in primary progressive aphasia variants. *Brain* **140**, 2737–2751 (2017).

53. McKhann, G. M. *et al.* The diagnosis of dementia due to alzheimer's disease: Recommendations from the national institute on aging-alzheimer's association workgroups on diagnostic guidelines for alzheimer's disease. *Alzheimer's & dementia* **7**, 263–269 (2011).

54. Albert, M. S. *et al.* The diagnosis of mild cognitive impairment due to alzheimer's disease: recommendations from the national institute on aging-alzheimer's association workgroups on diagnostic guidelines for alzheimer's disease. *Alzheimer's & dementia* **7**, 270–279 (2011).

55. Gaser, C., Dahnke, R. *et al.* Cat-a computational anatomy toolbox for the analysis of structural mri data. *Hbm* **2016**, 336–348 (2016).

56. Penny, W. D., Friston, K. J., Ashburner, J. T., Kiebel, S. J. & Nichols, T. E. *Statistical parametric mapping: the analysis of functional brain images* (Elsevier, 2011).

57. Sekihara, K. *et al.* Dual signal subspace projection (dssp): a novel algorithm for removing large interference in biomagnetic measurements. *J. neural engineering* **13**, 036007 (2016).

58. Cai, C. *et al.* Evaluation of a dual signal subspace projection algorithm in magnetoencephalographic recordings from patients with intractable epilepsy and vagus nerve stimulators. *Neuroimage* **188**, 161–170 (2019).

59. Ablin, P., Cardoso, J.-F. & Gramfort, A. Faster independent component analysis by preconditioning with hessian approximations. *IEEE Transactions on Signal Process.* **66**, 4040–4049 (2018).

60. Nolte, G. The magnetic lead field theorem in the quasi-static approximation and its use for magnetoencephalography forward calculation in realistic volume conductors. *Phys. Medicine & Biol.* **48**, 3637 (2003).

61. Sekihara, K., Nagarajan, S. S., Poeppel, D. & Marantz, A. Asymptotic snr of scalar and vector minimum-variance beamformers for neuromagnetic source reconstruction. *IEEE transactions on biomedical engineering* **51**, 1726–1734 (2004).

62. Sekihara, K. & Nagarajan, S. S. *Adaptive spatial filters for electromagnetic brain imaging* (Springer Science & Business Media, 2008).

63. Oostenveld, R., Fries, P., Maris, E. & Schoffelen, J.-M. Fieldtrip: open source software for advanced analysis of meg, eeg, and invasive electrophysiological data. *Comput. intelligence neuroscience* **2011** (2011).

64. Xia, M., Wang, J. & He, Y. Brainnet viewer: a network visualization tool for human brain connectomics. *PloS one* **8**, e68910 (2013).

65. Engels, M. *et al.* Slowing of hippocampal activity correlates with cognitive decline in early onset alzheimer's disease. an meg study with virtual electrodes. *Front. human neuroscience* **10**, 238 (2016).

66. Hipp, J. F., Hawellek, D. J., Corbetta, M., Siegel, M. & Engel, A. K. Large-scale cortical correlation structure of spontaneous oscillatory activity. *Nat. neuroscience* **15**, 884–890 (2012).

67. Sekihara, K. & Nagarajan, S. S. *Electromagnetic brain imaging: a bayesian perspective* (Springer, 2015).

68. Briels, C. T. *et al.* In pursuit of a sensitive eeg functional connectivity outcome measure for clinical trials in alzheimer's disease. *Clin. Neurophysiol.* **131**, 88–95 (2020).

69. Wiesman, A. I. *et al.* Spatio-spectral relationships between pathological neural dynamics and cognitive impairment along the alzheimer's disease spectrum. *Alzheimer's & Dementia: Diagn. Assess. & Dis. Monit.* **13**, e12200 (2021).

70. Benjamini, Y. & Hochberg, Y. Controlling the false discovery rate: a practical and powerful approach to multiple testing. *J. Royal statistical society: series B (Methodological)* **57**, 289–300 (1995).

Acknowledgements

The authors thank all the study participants for their support to our research. This work was supported from the following grants: R01AG062196 (SSN), R01NS100440 (SSN), R01DC017091 (SSN), P50DC019900 (SSN), UCOP-MRP-17-454755 (SSN), NIA P30-AG062422 (GDR, BLM), an industry research contract from Ricoh MEG Inc (SSN, HEK), K23 AG038357 (KV), a grant from John Douglas French Alzheimer's Foundation (KV), the S.D. Bechtel Jr. Foundation (KV), Alzheimer's Association grant PCTRB-13-288476 made possible by Part the Cloud™ (KV), K08AG058749 (KGR), 1R21AG077498-01 (KGR), Larry L. Hillblom Foundation grant 2015-A-034-FEL (KGR), 2019-A-013-SUP (KGR), Alzheimer's Association grant AARG-21-849773 (KGR), and R21AG077498-01 (KGR).

Author contributions

K.K, K.G.R, and S.S.N together designed this study and analyses, analyzed and interpreted the data, and developed the manuscript. H.M, F.S, and H.E.K contributed to data interpretation. K.S contributed to the development of

data analyses. K.P.R, B.L.M, J.H.K, G.D.R, and K.V contributed to manuscript editing. All authors reviewed the manuscript.

Additional information

Competing interests

K.K. and H.M. are employees of Ricoh Company, Ltd. The authors declare that no other competing interests exist. The other authors declare no competing financial conflicts of interest to disclose.

Data availability

The informed consent did not include a declaration regarding public availability of data, and the data for this study will not be made publicly available. Anonymized data may be shared on request from qualified investigators for the purposes of replicating procedures and results within the limits of participants' consent. Matlab scripts used in this study are available from the corresponding author upon reasonable request from qualified researchers.

List of Figures

1 **Atrophy-cognition EBM staging of AD progression**. (a) Group comparison of PHG volumes [$t(143) = -9.508$; $^{***}p < 0.001$]. (b) Histogram of PHG volume loss z-scores. Higher z-scores denote more severity as the z-scores were defined with a negative sign. (c) Group comparison of MMSE scores [$t(144) = -10.171$; $^{***}p < 0.001$]. (d) Histogram of MMSE-decline z-scores defined with a negative sign. (e) The ratio of subjects categorized to each stage; blue: Control (CDR= 0), orange: MCI due to AD (CDR= 0.5), pink: mild AD dementia (CDR= 1), and red: moderate AD dementia (CDR= 2). (f) Distribution of the stages in PHG volume loss versus MMSE score plot. Colors of the dots denote the seven stages. A star symbol denotes weighted means of z_{PHG} and MMSE scores for stage 4: $z_{\mathrm{PHG}} = 1.33(\pm 0.258)$ and MMSE= $26.3(\pm 0.82)$. The values in the parenthesis denote the standard error (SE) of the weighted means. (g) Trajectories of PHG volume loss and MMSE score as a function of the seven stages. Weighted means ($\pm$ SE) are displayed. (h) Progression of GM volume loss (z-scores) from stage 1 to 7. The regional GM atrophy in the MCI stage (stage 4) was circled with dotted lines. 27

2 **Profiles of neural synchrony as a function of the AD stages estimated by AC-EBM** . (a,b) Profiles of AEC (a) and spectral power (b) as a function of the seven stages, showing weighted means ($\pm$ SE). Neural synchrony monotonously increased with AD progression in delta-theta band and monotonously decreased in alpha and beta bands. (c,d) Regional AEC (c) and spectral power (d) as a function of the seven stages. Deviations from the neural synchrony spatial patterns averaged over controls are displayed. The deviations were obtained by computing weighted means of the z-scores standardized by the controls for each stage. The spatial patterns in the MCI stage (stage 4) were circled with dotted lines. (e,f) Changes in neural synchrony during preclinical stages. Regional comparisons between two stages (stages 4 vs 1) based on non-parametric tests of the weighted mean differences δz are shown. The differences exceeding threshold (FDR-corrected p-value $q < 0.05$) are displayed. There was no significant difference in delta-theta-band long-range synchrony. 28

3 **Trajectories of long-range neural synchrony in delta-theta, alpha, and beta-bands from SAC-EBMs**. (a,e,i) The ratio of subjects categorized to each stage. (b,f,j) Trajectories of long-range synchrony, PHG volume loss, and MMSE score change as a function of the ten stages, showing weighted means ($\pm$ SE). Asterisks ($^{*}q < 0.05$ and $^{***}q < 0.001$, FDR corrected) denote statistical significance in comparisons between stages 5 vs 1. All pairs of stages with significant weighted-mean differences were listed in Supplementary Table 7. (c,g,k) Regional long-range synchrony along the stages. The deviations from the regional patterns of the control group are displayed. The regional patterns at the onset of the MCI stage were circled with dotted lines. (d,h,l) Changes in regional patterns during preclinical stages. Regional comparisons between two stages based on non-parametric tests of the weighted mean differences δz are shown. The differences exceeding threshold ($q < 0.05$, FDR corrected) are displayed. 29

4 **Trajectories of local neural synchrony in delta-theta, alpha and beta bands from SAC-EBMs**. (a,e,i) The ratio of subjects categorized to each stage. (b,f,j) Trajectories of local synchrony, PHG volume loss, and MMSE score change as a function of the 10 stages, showing weighted means ($\pm$ SE). Asterisks ($^{***}q < 0.001$, FDR corrected) denote statistical significance in comparisons between stages 6 vs 1. All pairs of stages with significant weighted-mean differences were listed in Supplementary Table 9. (c,g,k) Regional spectral power along the stages. The deviations from the regional patterns of the control group are displayed. The regional patterns in the onset of the MCI stages were circled with dotted lines. (d,h,l) Changes in regional patterns during preclinical stages. Regional comparisons between two stages based on non-parametric tests of the weighted mean differences δz are shown. The differences exceeding threshold ($q < 0.05$, FDR corrected) are displayed. 30

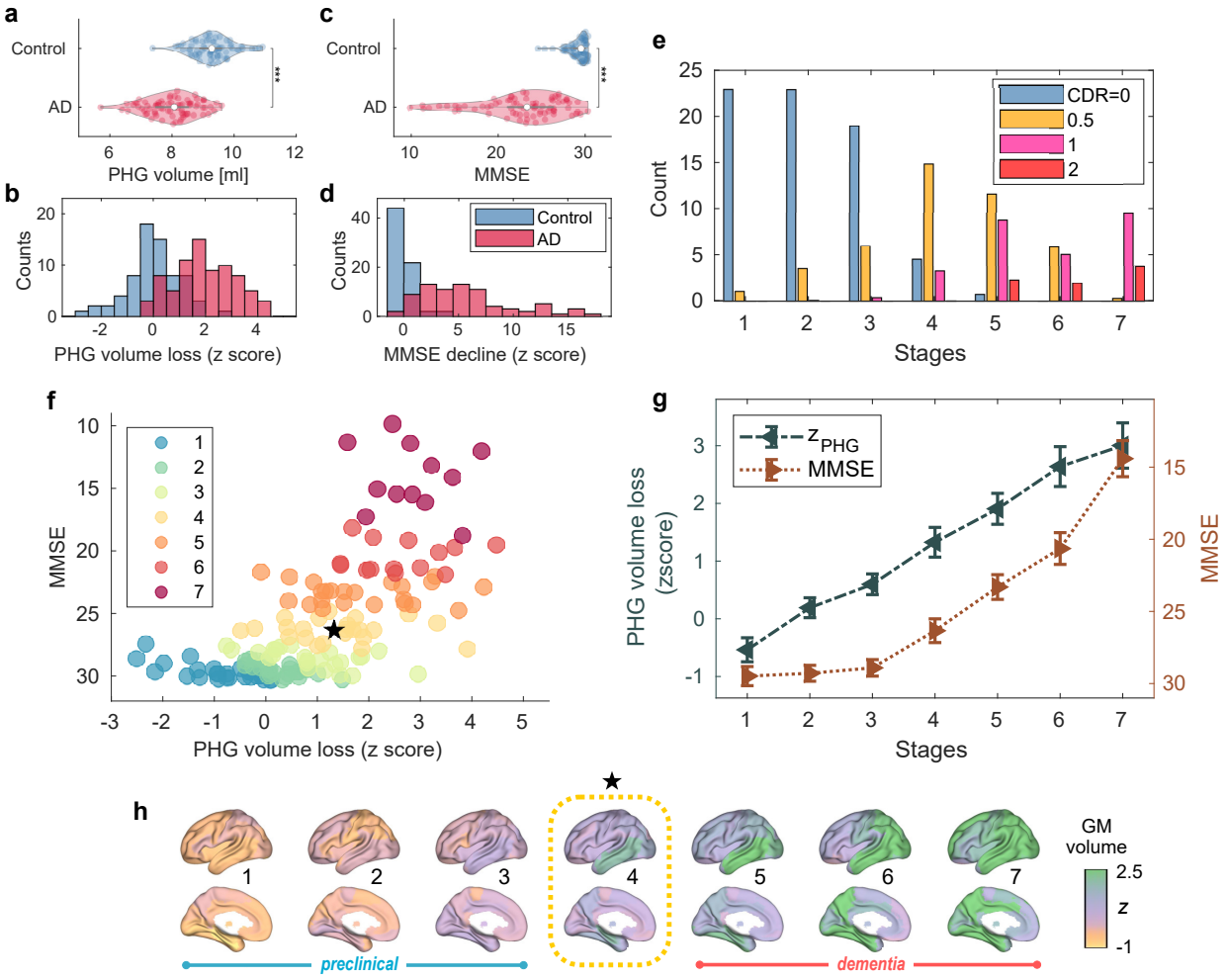

Figure 1. Atrophy-cognition EBM staging of AD progression. (a) Group comparison of PHG volumes [$t(143) = -9.508$; $^{***}p < 0.001$]. (b) Histogram of PHG volume loss z-scores. Higher z-scores denote more severity as the z-scores were defined with a negative sign. (c) Group comparison of MMSE scores [$t(144) = -10.171$; $^{***}p < 0.001$]. (d) Histogram of MMSE-decline z-scores defined with a negative sign. (e) The ratio of subjects categorized to each stage; blue: Control (CDR$=0$), orange: MCI due to AD (CDR$=0.5$), pink: mild AD dementia (CDR$=1$), and red: moderate AD dementia (CDR$=2$). (f) Distribution of the stages in PHG volume loss versus MMSE score plot. Colors of the dots denote the seven stages. A star symbol denotes weighted means of z_{PHG} and MMSE scores for stage 4: $z_{\mathrm{PHG}} = 1.33(\pm 0.258)$ and MMSE$= 26.3(\pm 0.82)$. The values in the parenthesis denote the standard error (SE) of the weighted means. (g) Trajectories of PHG volume loss and MMSE score as a function of the seven stages. Weighted means ($\pm$ SE) are displayed. (h) Progression of GM volume loss (z-scores) from stage 1 to 7. The regional GM atrophy in the MCI stage (stage 4) was circled with dotted lines.

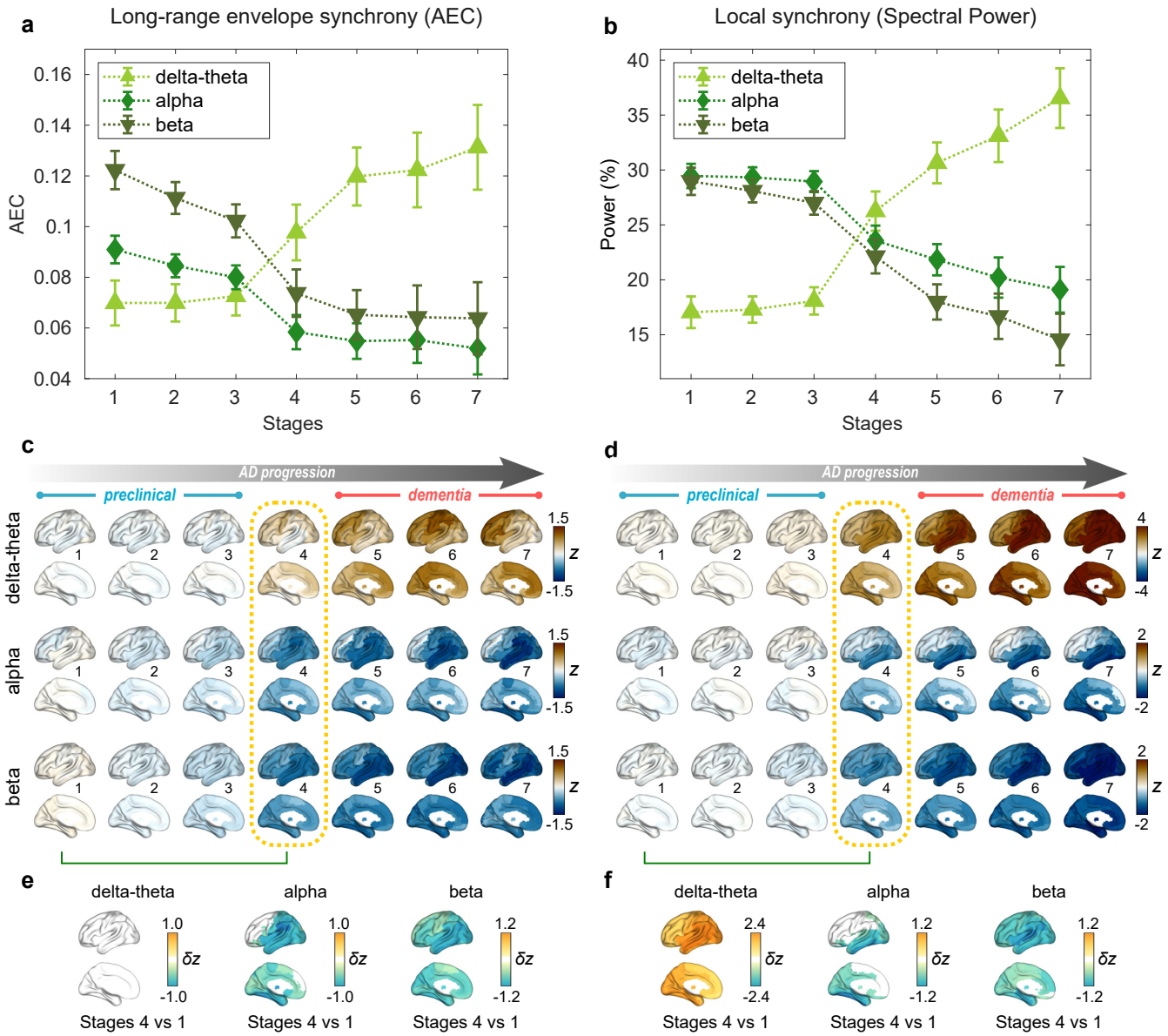

Figure 2. Profiles of neural synchrony as a function of the AD stages estimated by AC-EBM . (a,b) Profiles of AEC (a) and spectral power (b) as a function of the seven stages, showing weighted means (± SE). Neural synchrony monotonously increased with AD progression in delta-theta band and monotonously decreased in alpha and beta bands. (c,d) Regional AEC (c) and spectral power (d) as a function of the seven stages. Deviations from the neural synchrony spatial patterns averaged over controls are displayed. The deviations were obtained by computing weighted means of the z-scores standardized by the controls for each stage. The spatial patterns in the MCI stage (stage 4) were circled with dotted lines. (e,f) Changes in neural synchrony during preclinical stages. Regional comparisons between two stages (stages 4 vs 1) based on non-parametric tests of the weighted mean differences δz are shown. The differences exceeding threshold (FDR-corrected p-value $q < 0.05$) are displayed. There was no significant difference in delta-theta-band long-range synchrony.

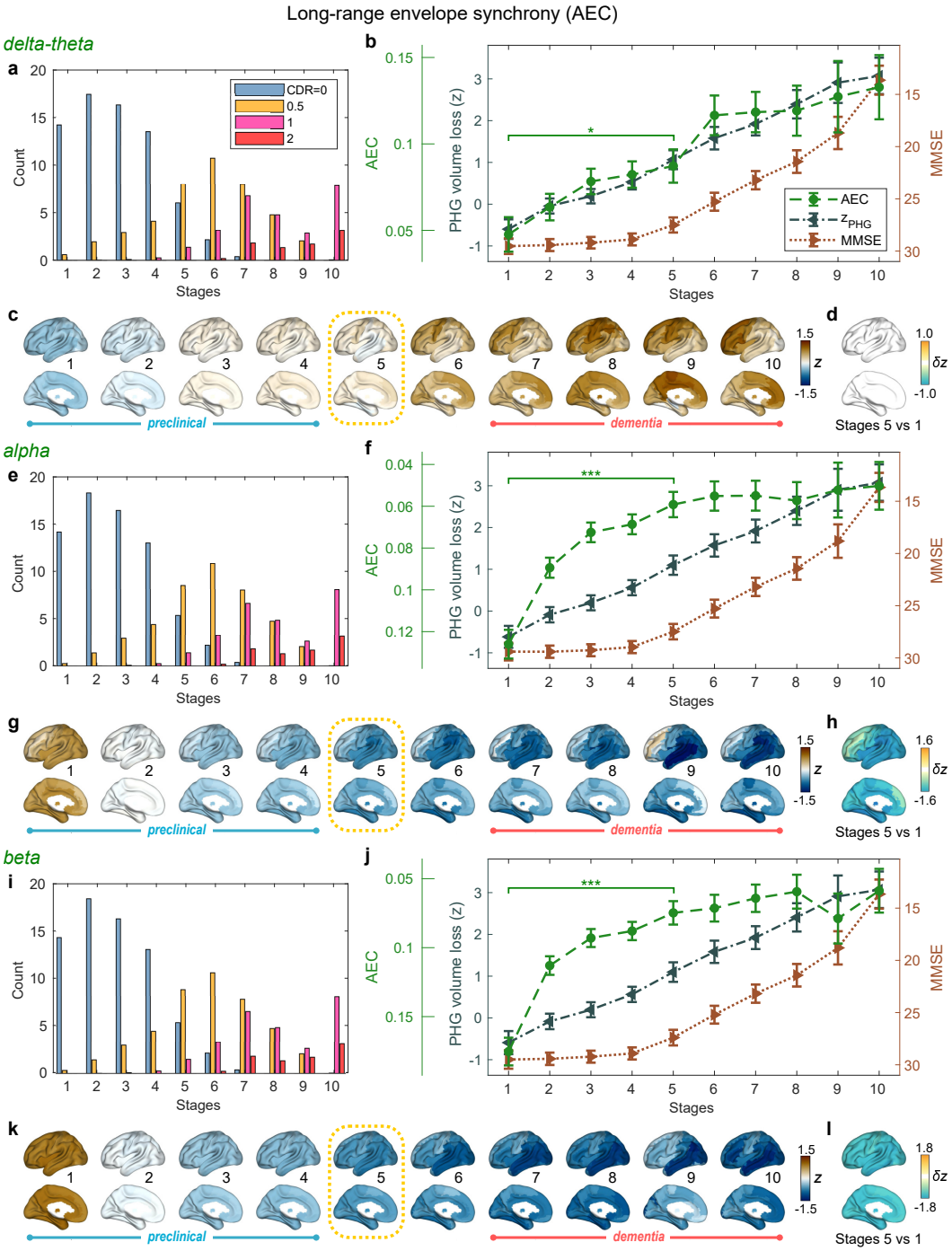

Figure 3. Trajectories of long-range neural synchrony in delta-theta, alpha, and beta-bands from SAC-EBMs. (a,e,i) The ratio of subjects categorized to each stage. (b,f,j) Trajectories of long-range synchrony, PHG volume loss, and MMSE score change as a function of the ten stages, showing weighted means ($\pm$ SE). Asterisks ($^{*}q < 0.05$ and $^{***}q < 0.001$, FDR corrected) denote statistical significance in comparisons between stages 5 vs 1. All pairs of stages with significant weighted-mean differences were listed in Supplementary Table 7. (c,g,k) Regional long-range synchrony along the stages. The deviations from the regional patterns of the control group are displayed. The regional patterns at the onset of the MCI stage were circled with dotted lines. (d,h,l) Changes in regional patterns during preclinical stages. Regional comparisons between two stages based on non-parametric tests of the weighted mean differences δz are shown. The differences exceeding threshold ($q < 0.05$, FDR corrected) are displayed.

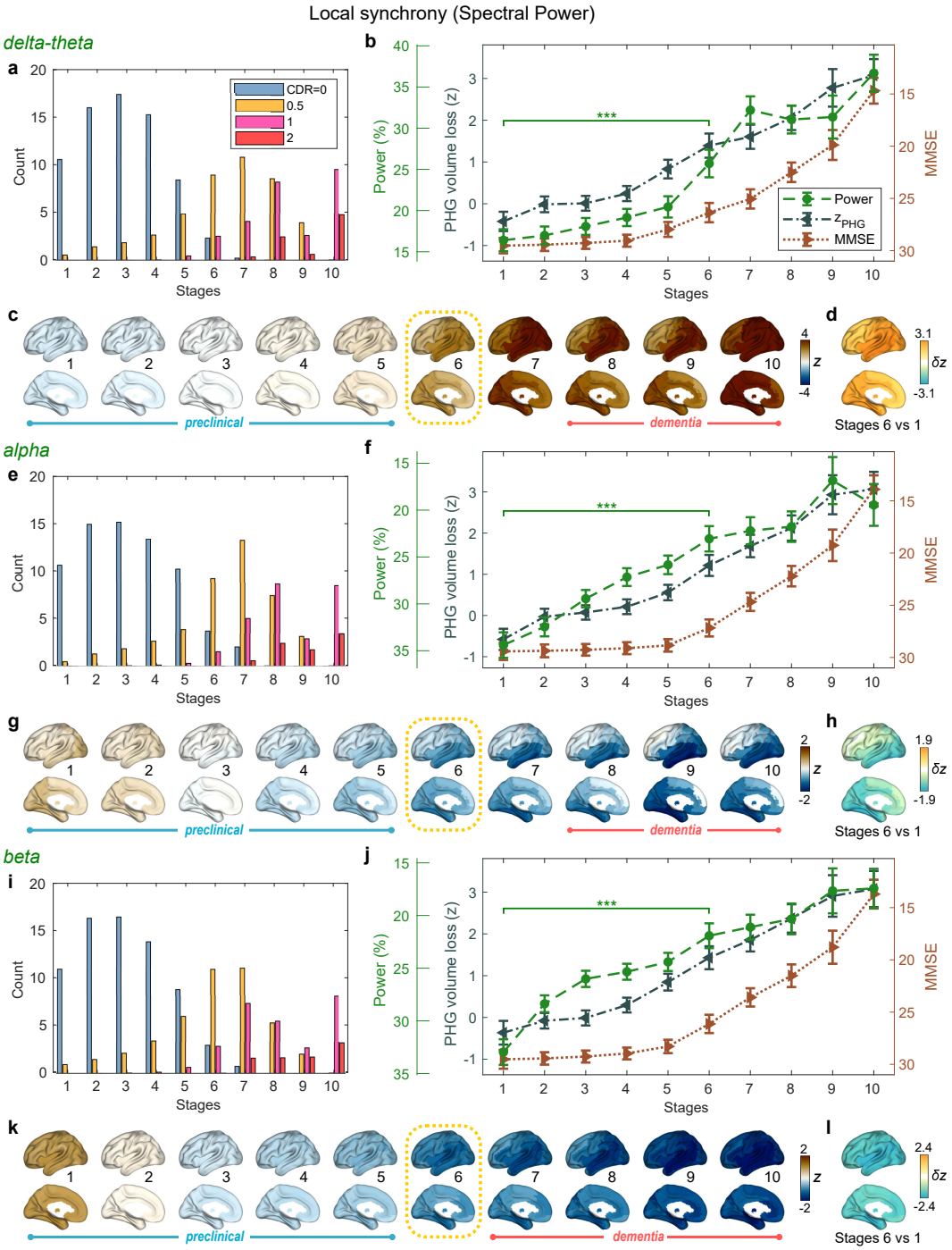

Figure 4. Trajectories of local neural synchrony in delta-theta, alpha and beta bands from SAC-EBMs. (a,e,i) The ratio of subjects categorized to each stage. (b,f,j) Trajectories of local synchrony, PHG volume loss, and MMSE score change as a function of the 10 stages, showing weighted means ($\pm$ SE). Asterisks ($^{***}q < 0.001$, FDR corrected) denote statistical significance in comparisons between stages 6 vs 1. All pairs of stages with significant weighted-mean differences were listed in Supplementary Table 9. (c,g,k) Regional spectral power along the stages. The deviations from the regional patterns of the control group are displayed. The regional patterns in the onset of the MCI stages were circled with dotted lines. (d,h,l) Changes in regional patterns during preclinical stages. Regional comparisons between two stages based on non-parametric tests of the weighted mean differences δz are shown. The differences exceeding threshold ($q < 0.05$, FDR corrected) are displayed.